



CHALMERS
UNIVERSITY OF TECHNOLOGY

An improved procedure for strongly coupled prediction of sailing yacht performance

Downloaded from: <https://research.chalmers.se>, 2025-05-09 17:58 UTC

Citation for the original published paper (version of record):

Persson, A., Larsson, L., Finnsgård, C. (2021). An improved procedure for strongly coupled prediction of sailing yacht performance. *Journal of Sailing Technology*, 6(1): 133-150.
<http://dx.doi.org/10.5957/jst/2021.6.1.133>

N.B. When citing this work, cite the original published paper.

An Improved Procedure for Strongly Coupled Prediction of Sailing Yacht Performance

A. Persson

SSPA Sweden AB and Chalmers University of Technology, Sweden, adam.persson@sspa.se

L. Larsson

Chalmers University of Technology, Sweden

C. Finnsgård

SSPA Sweden AB, Sweden

Manuscript received December 3, 2020; revision received May 28, 2021; accepted June 22, 2021.

Abstract. In this paper, an improved procedure for strongly coupled prediction of sailing yacht performance is developed. The procedure uses 3D RANS CFD to compute the hydrodynamic forces. When coupled to a rigid body motion solver and a sail force model, along with a rudder control algorithm, this allows sailing yacht performance to be predicted within CFD software. The procedure provides improved convergence when compared to a previously published method. The grid motion scheme, partially using overset grid techniques, means that correct alignment between the free surface and the background grid is ensured even at large heel angles. The capabilities are demonstrated with performance predictions for the SYRF 14 m yacht, at one true wind speed, over a range of true wind angles, with up- and downwind sailsets. The results are compared to predictions from the ORC-VPP for a yacht with similar main particulars.

Keywords: Computational Fluid Dynamics; Velocity Prediction Program; Six Degrees of Freedom; Overset Mesh.

NOMENCLATURE

A	Sail area [m ²]
A_J	Jib area [m ²]
A_M	Mainsail area [m ²]
A_{SP}	Spinnaker area [m ²]
B	Beam [m]
BAS	Boom height [m]
c_i	Sail chord length [m]
C_L	Lift coefficient [–]
C_{D0}	Parasitic drag coefficient [–]
C_{DI}	Induced drag coefficient [–]
C_{DQ}	Quadratic parasitic drag coefficient [–]
C_u	Thrust coefficient [–]
C_v	Side force coefficient [–]
E	Mainsail foot length [m]
F_u	Thrust [N]
F_v	Side force [N]

I_J	Foretriangle height [m]
I_{SP}	Spinnaker halyard height [m]
J	Foretriangle base [m]
LOA	Length over all [m]
m	Mass [kg]
m_C	Crew mass [kg]
MHB	Mainsail head width [m]
P	Mainsail hoist length [m]
S	Sailplan span [m]
T	Draft [m]
V_A	Apparent wind speed [m s^{-1}]
V_B	Boat velocity [m s^{-1}]
V_i	Velocity in a coordinate system component [m s^{-1}]
V_T	True wind speed [m s^{-1}]
β_A	Apparent wind angle [$^\circ$]
β_T	True wind angle [$^\circ$]
δ	Rudder angle [$^\circ$]
λ	Leeway angle [$^\circ$]
Λ_E	Effective aspect ratio [–]
μ_w	Dynamic viscosity, water [Pa s]
ϕ	Heel angle [$^\circ$]
ρ_a	Density, air [kg m^{-3}]
ρ_w	Density, water [kg m^{-3}]
θ	Trim angle [$^\circ$]
p, q, r	Rudder axis coordinate system
u, v, w	Body-fixed coordinate system
u', v', w'	CE-fixed coordinate system
x, y, z	Space-fixed coordinate system
CE	Aerodynamic centre of effort
CG	Centre of gravity
CLR	Centre of lateral resistance
CP	Crew position
DOF	Degree of Freedom
LE	Leading edge
TE	Trailing edge

1. INTRODUCTION

Prediction of sailing vessel performance remains a central topic in both industry and academia. Different approaches have been suggested over the years, ranging from generalised and efficient static programs to complex dynamic programs.

Simplified procedures deliver generalised results at low computational cost, but with reduced accuracy. In addition, it is difficult to model novel configurations, such as hydrofoils, where non-linear interactions may occur. Advanced procedures can model performance from first-principle physics, considering the detailed design. However, these suffer from increased computational cost and reduced generality.

The state-of-art approach to performance prediction solves the rigid body motion equations, using forces from pre-computed matrices, which must be defined over an extended operating range to ensure successful interpolation.

With the ever-increasing complexity of contemporary rig and appendage configurations, the size of the force-matrices increases rapidly. In addition, if vessel dynamics are to be simulated, this further increases the matrix size, up to the point where pre-computation becomes impractical.

An alternative approach is to solve the rigid body equations along with the RANS-equations, in a strongly coupled manner, by time-stepping the solution from a starting guess until steady-state convergence has been reached, removing the need for pre-computed matrices and interpolation. The concept has been demonstrated previously, by Roux et al. (2008), Azcueta and Schutt (2010), Boehm and Graf (2010) and Levin and Larsson (2017).

Roux et al. (2008) presented 5DOF simulations for an AC90 yacht, with a pre-computed sail force applied. The hydrodynamic and aerodynamic solution methods are described in detail, but very few details on the coupling are presented. The coupled procedure seems to completely neglect the yaw moment equation, meaning that the yacht may be imbalanced in the simulated condition. The procedure used appears to result in slow convergence to steady state, with some oscillations still remaining after 150 s of simulated time.

Azcqueta and Schutt (2010) presented results from 5- and 6DOF strongly coupled simulations, again using pre-computed sail forces. The authors describe the importance of achieving yaw moment equilibrium, noting that significant differences in boat speed were found when comparing 5- and 6DOF simulations. This requires an adjustable rudder and a rudder controller. The results shown indicate that a steady-state solution could be found in a reasonable simulated time.

Boehm and Graf (2010) and Levin and Larsson (2017) both present detailed descriptions of the coupled simulation setup. However, these implementations show poor convergence to steady-state, either requiring extended simulation time to reach convergence, or converging to an oscillating state. In an attempt to improve convergence, Levin and Larsson (2017) presented an advanced initialisation procedure, which increases simulation runtime and requires manual intervention by the user. Both Boehm and Graf (2010) and Levin and Larsson (2017) also noted that the free surface discretisation becomes poor at high heel angles, when alignment between grid and free surface is lost.

The purpose of this paper is to further develop the procedure for strongly coupled prediction of sailing yacht performance. The procedure provides improved convergence compared to the method presented by Levin and Larsson (2017), which was achieved by implementing an integral rudder controller, along with wave damping boundary conditions and an improved grid motion setup. In addition, the improved grid motion setup allows the grid to stay aligned with the free surface, improving free surface discretisation and reducing numerical artefacts.

1.1 Demonstration Case

The SYRF 14 m yacht (Sailing Yacht Research Foundation, 2017) was chosen as a test case. It is representative of a modern, high-performance keel boat, and it is suitable as a test case for velocity prediction programs, since hull, appendage and sail plan geometries are defined.

In Figure 1, a lines plan of the SYRF 14 m yacht is shown. In Table 1, the main particulars of the boat are given. The centre of gravity (CG) coordinates are given for the initial condition, and in the global coordinate system (see section 2.1.1).

Figure 2 shows the sailplan drawing of the yacht. The sailplan of the yacht has a mainsail, a jib and an asymmetric spinnaker. The centre of effort (CE) for each sail is indicated with a coloured dot. Selected sailplan dimensions are given in Table 2. The measurements are defined according to ORC (2017).

Two sailsets are considered. One upwind sailset, which is used for true wind angles β_T between $30 - 120^\circ$, consisting of mainsail and jib; and one downwind sailset, used for true wind angles β_T between $90 - 165^\circ$, consisting of mainsail and asymmetric spinnaker.

Table 1: Particulars of the SYRF 14 m yacht

LOA [m]	B [m]	T [m]	m [kg]	m_c [kg]
14.0	4.2	3.36	7384	960
CG_x [m]	CG_y [m]	CG_z [m]	CP_u [m]	CP_v [m]
-7.536	0.0	1.0	0.0	-1.68

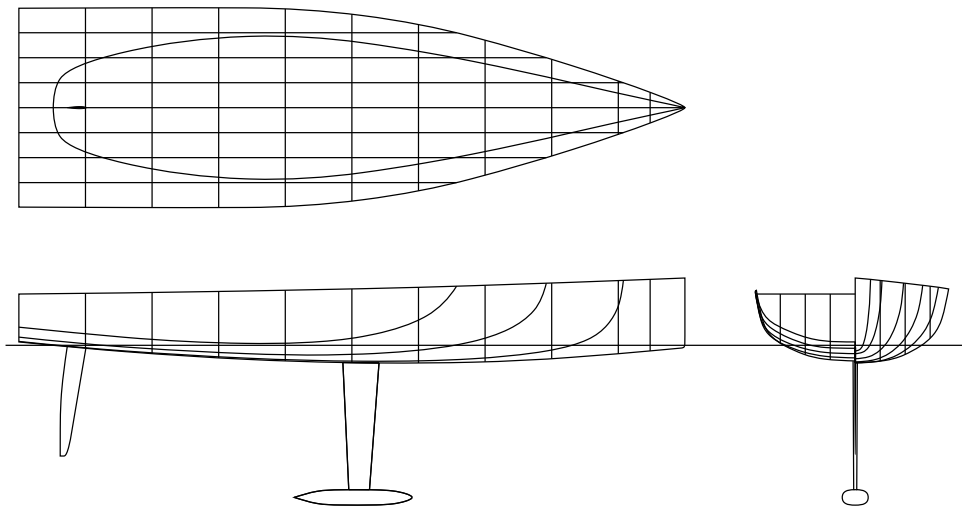
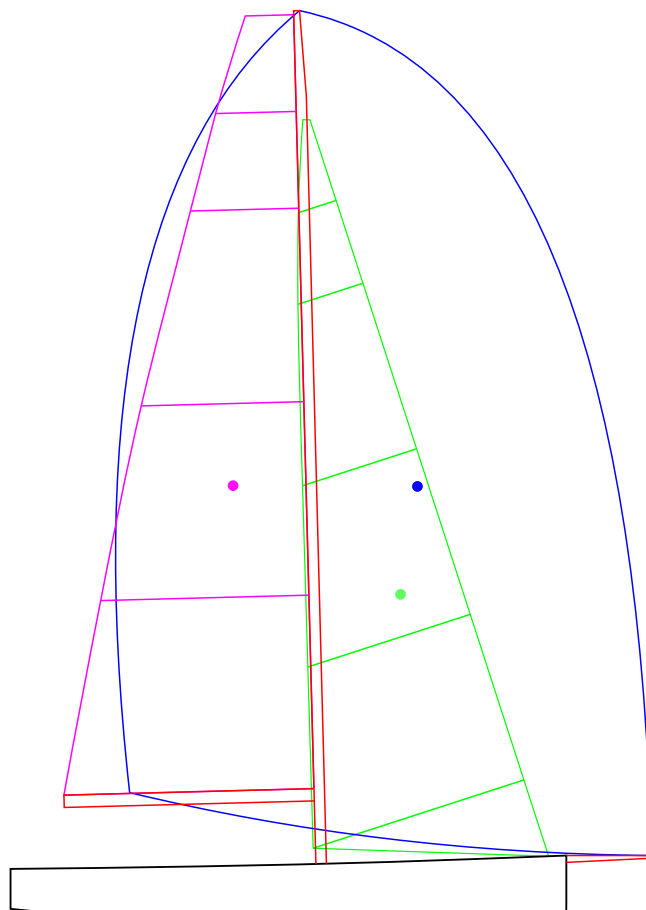


Figure 1: Lines plan of the SYRF 14 m yacht

Table 2: Sailplan dimensions of the SYRF 14 m yacht

P [m]	BAS [m]	E [m]	HB [m]	J [m]
19.5	1.9	6.3	1.2	5.6
I_J [m]	I_{SP} [m]	A_M [m ²]	A_J [m ²]	A_{SP} [m ²]
19	21.5	77.3	59.9	238.2

**Figure 2: Sail plan of the SYRF 14 m yacht**

2. METHOD

The CFD-VPP implementation can be divided in two parts. The first part is a CFD software, acting as a host for the VPP procedure. The CFD software solves the hydrodynamic forces and rigid body motions of the yacht.

The second part is the performance prediction routine, which includes a sail force model, rudder control algorithm and initialisation procedures.

By solving these two in a closely coupled manner in the time domain, stepping until equilibrium has been reached, it is possible to predict the steady-state 6DOF velocity and orientation for a specific yacht and operating condition.

Over the operating range, a yacht will sail at widely differing speeds, with different leeway angles and changing orientations in pitch and heel. This wide range of motion makes CFD simulations challenging, since a valid grid configuration must be maintained over the entire range of motion.

Overset grid methods allow large amplitude motions to be resolved, by using overlapping grids moving relative to each other. This is a critical factor for successful implementation of a CFD-VPP.

2.1 CFD Simulation Setup

2.1.1 Coordinate Systems

Four different coordinate systems are used in the simulation setup. A graphical overview is shown in Figure 3. A global, space-fixed coordinate system (x, y, z) is defined. In the initial state, the origin coincides with the forward perpendicular. It is oriented so that the x - y plane is aligned with the undisturbed free surface, with the z -axis oriented in the direction of the gravitational acceleration.

The rigid body motion is solved in a body-fixed coordinate system (u, v, w) , with the origin at the centre of gravity. In the initial position, u, v, w is aligned with x, y, z . A second body-fixed system (u', v', w') with the same orientation, but with the origin located in the centre of effort (CE) is used by the sail force model. The position of the CE varies depending on apparent wind angle β_A and sailset (see section 2.2.1).

A third body-fixed coordinate system (p, q, r) has the origin at the the hull surface/rudder shaft intersection. The q -axis is aligned with the v -axis, while the r -axis is aligned with the rudder shaft. The rudder rotates around the r -axis.

2.1.2 Computational Domain

The configuration of the computational domain is to a large degree determined by the need to account for relative motion between background domain and yacht, and between yacht and rudder. For this reason, the domain is divided into one background domain and two overset domains, one containing the yacht hull/keel and one containing the rudder.

The background domain is rectangular, with dimensions 70x56x21 m, corresponding to 5x4x1.5 *LOA*. The free surface is located so that 1 *LOA* of the domain is below the free surface, with 0.5 *LOA* above the free surface. The overset domains are fitted to the bounding box of the respective body, with a clearance of 0.5 m to the boundary of the domain. In figure 4 the overset domains are shown superimposed on the lines plan of the SYRF 14 m yacht.

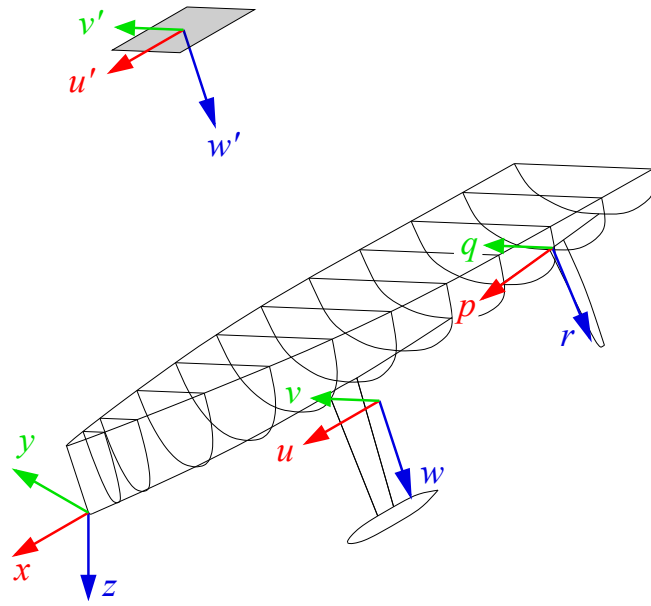


Figure 3: Global and local coordinate systems

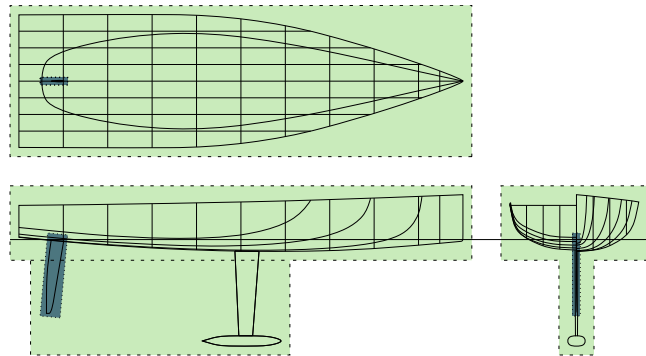


Figure 4: Hull overset domain (green) and rudder overset domain (blue)

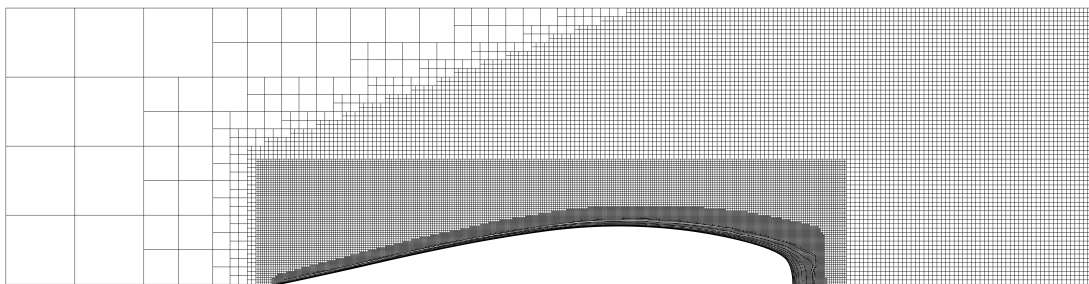


Figure 5: Nearfield waterplane grid detail. Only half of the domain is shown.

2.1.3 Grid Configuration

The background grid and the two overset grids, are of hexahedral, unstructured type. The background grid is volumetrically refined around the free surface and the overset domains.

In proximity to the free surface, the grid is anisotropically refined, with smaller cells in the vertical (z) direction. The region covers the entire domain in the x - and y -direction, and extends ± 0.5 m from the initial free surface position. In addition, the grid is further refined in the x - and y -direction, in the so called 'Kelvin wedge' region, to resolve the wave pattern formed by the hull.

Around the overset interface, the background grid has to be isotropically refined to ensure that a consistent cell size is maintained across the overset interface. The refinement region is sized to allow the yacht to move over the expected range of motion, without any part of the overset domain extending outside the refined region. The critical DOF is heel, with a maximum permissible heel angle of 30° .

In the hull overset domain, the hull surface cell size follows from what is imposed in the background grid overset interface refinement. The grid on the keel blade and bulb is refined, with further refinements to capture details around the leading/trailing edges and keel/hull intersection. A region surrounding the rudder overset interface is also refined, similarly to the background domain, allowing $\pm 15^\circ$ rudder angle while maintaining a consistent cell size across the interface. Figure 5 shows a detail view of the grid in the waterplane. Only half of the computational domain is shown.

In the rudder overset domain, the surface size again follows the size imposed in the overset interface refinement, with additional refinement on the leading/trailing edge. Surrounding the intersection between the rudder blade and hull, the grid is refined to resolve the gap between rudder and hull. The cell sizes in the refinement zones are given as a fraction of length over all (LOA), in tables 3 and 4.

Table 3: Volume refinements: cell size given as LOA/n

Region	$n [-]$		
	x	y	z
Free surface, global	–	–	500
Free surface, near-field	125	125	500
Hull overset interface	250	250	500
Rudder overset interface	1000	1000	1000

Table 4: Isotropic surface refinements: cell size given as LOA/n

Surface	$n [-]$
Hull	500
Keel blade and bulb	1000
Keel LE/TE	4000
Rudder blade	2000
Rudder LE/TE	8000

On all wall boundaries, prism layers are generated in order to resolve the velocity gradient in the boundary layer. The prism layers are adapted to the different boundary layer scales seen on the hull, keel blade, keel bulb and rudder. Detailed prism layer specifications are given in Table 5.

The total number of cells in the grid is $17.4 \cdot 10^6$. A considerable amount of cells are generated in the volumetric refinements that are required to ensure consistent cell sizes across the overset

Table 5: Prism layer specifications

Surface	Y^+	Δs [m]	N_{PL}	T_{PL} [m]
Hull	60	$8 \cdot 10^{-4}$	8	0.144
Keel blade	60	$4 \cdot 10^{-4}$	8	0.014
Keel bulb	60	$5 \cdot 10^{-4}$	8	0.036
Rudder	60	$3 \cdot 10^{-4}$	8	0.008

interfaces. Some of these cells become inactive when the simulation is running. The number of active cells in the initial state is $15.1 \cdot 10^6$.

2.1.4 Numerical Setup and Physical Models

An implicit unsteady, segregated solver is used, with a SIMPLE pressure-velocity coupling scheme and a constant time step of 0.1 s. The free surface is modeled using the volume-of-fluid (VOF) method. The fluids are modeled as incompressible. The physical properties are shown in Table 6.

Table 6: Physical properties

ρ_a [kg m^{-3}]	ρ_w [kg m^{-3}]	μ_w [Pa s]	g [m s^{-2}]
1.18415	1026.021	$1.85508 \cdot 10^{-5}$	9.81

The two-equation SST Menter K-Omega turbulence model is used. While laminar to turbulent transition is an important consideration in the design of appendages for sailing yachts, no transition model is used in the simulations presented here. Thus, the flow is considered to be fully turbulent.

A high Y^+ wall treatment is used, equivalent to a traditional wall-function approach. This is used in order to reduce the demands on near-wall resolution, allowing a significant reduction in grid size in comparison to a low Y^+ , wall resolved approach.

In order to prevent wave reflection on the inlet, outlet and side boundaries, wave damping is used. The waves are dampened by introducing a resistance term to the z -momentum equation, The approach used follows that from Choi and Yoon (2009). The wave damping term is applied within a zone 7 m from each boundary.

The use of overset grids means that field values must be exchanged on the interface, i.e. for each acceptor cell in the overset grid, a number of donor cells in the background grid must be identified, and then the field value is interpolated between them. A linear interpolation scheme is used for this.

2.1.5 Rigid Body Motions

The computation of the rigid body motion in response to the hydro- and aerodynamic forces is handled by the 6DOF solver that is integrated in the CFD software. The yacht is free to move in five degrees of freedom; surge, sway, heave, roll, pitch, but fixed in yaw. Yaw moment equilibrium is instead ensured by adjusting the rudder angle, see section 2.2.4.

In contrast to the approach used by Boehm and Graf (2010) and Levin and Larsson (2017), the translational and rotational components of the motion are treated separately. The translational components are treated as a rigid body motion of the entire domain, including background, hull and rudder domains. Thus, no relative translation occurs between the domains, allowing the size of the computational domain to be minimised.

The rotational motion components are resolved using overset grid motion. As the yacht rotates in pitch and roll, the hull and rudder overset domains rotate relative to the background domain, which

remains aligned with the global coordinate system and the free surface. Since an anisotropic grid is used to resolve the free surface, correct alignment between the grid and free surface is critical.

2.2 Performance Prediction Algorithm

In addition to the base CFD configuration, additional routines are required for performance prediction, such as a sail force model and rudder control algorithms. In this section, these routines are described.

VPP programs commonly use depowering functions, such as flattening, twisting and reefing, to reduce sail force and CE height when the heeling moment becomes too large. In the current implementation, no such depowering functions are used.

2.2.1 Estimating Centre of Effort

The position of the aerodynamic center of effort CE in relation to the centre of lateral resistance CLR , has a significant effect on the performance of a sailing vessel. The centre of effort position is given in the body-fixed coordinate system u, v, w . The vertical position, CE_w , determines the heeling moment, while the longitudinal and transverse position (CE_u, CE_v) determines the yawing moment.

The vertical centre of effort of each sail, $CE_{w,i}$ is taken as the height of the area centroid of the sail. The chordwise centre of effort of each sail is assumed to be located at 35% of the chord length c_i from the leading edge, at the height of the area centroid. This is based on data from Larsson et al. (2014).

The effect of sheeting is modeled by projecting the assumed centre of effort in the longitudinal and transverse directions, with half the apparent wind angle, see equations 1 and 2, giving the longitudinal (CE_u) and transverse (CE_v) coordinates of the centre of effort. This is simplistic, but mimics the desired trend, with CE moving forward and to leeward with increasing apparent wind angle.

$$CE_{u,i} = LE_{u,i} + 0.35c_i \cos(\beta_A/2) \quad (1)$$

$$CE_{v,i} = 0.35c_i \sin(\beta_A/2) \quad (2)$$

The aggregate centre of effort coordinates (CE_u, CE_v, CE_w) is then computed as a sum of the individual centre of effort, weighted by the individual sail area and partial force coefficient, see Equation 3. This is a slight modification of the equation presented in ORC (2017), neglecting the *blanketing factor*.

$$CE = \frac{\sum CE_i \sqrt{C_{L,i}^2 + C_{D0,i}^2} A_i}{\sqrt{C_L^2 + C_{D0}^2} A} \quad (3)$$

In Figure 6, the aggregate CE coordinates are shown.

2.2.2 Computation of Apparent Wind

The true wind is defined in the global coordinate system x, y, z . For $\beta_A = 45^\circ$, the wind flows in negative x -direction and positive y -direction, corresponding to port tack.

For the apparent wind computation, the velocities in the u', v', w' coordinate system are used. These are taken in a plane located at the centre of effort CE (see section 2.1.1).

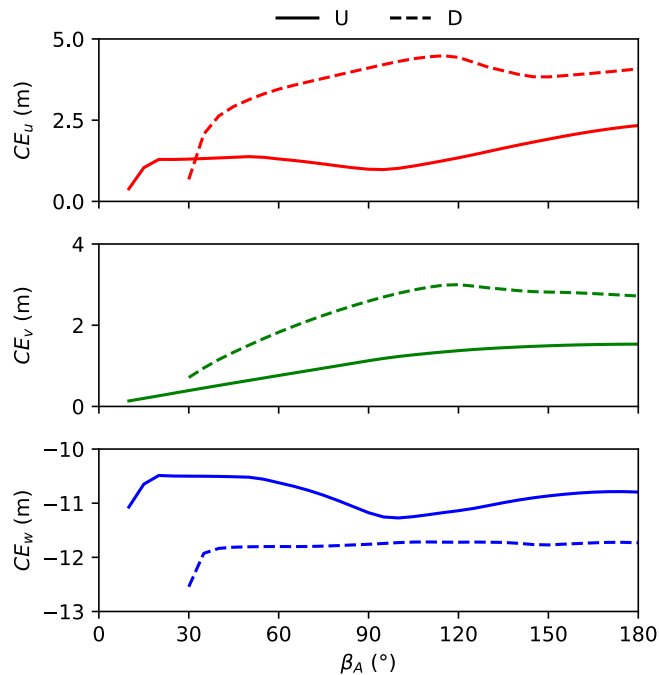


Figure 6: CE coordinates for up- and downwind sailsets

The apparent wind, β_A and V_A , is then computed as shown in equations 4 and 5.

$$\beta_A = \text{atan2}(V_T \sin \beta_T \cos \phi - V_{v'}, V_T \cos \beta_T \cos \theta + V_{u'}) \quad (4)$$

$$V_A = \sqrt{(V_T \sin \beta_T \cos \phi - V_{v'})^2 + (V_T \cos \beta_T \cos \theta + V_{u'})^2} \quad (5)$$

Computing the apparent wind as suggested above means that the effects of vessel pitch and heel motions are accounted for. Thus the sail model can be considered to be quasi-static.

2.2.3 Sail Force Model

The sail forces are modeled using empirical force coefficients from ORC (2017). The force coefficients are given in tabulated form, as a function of the apparent wind angle β_A , separately for each sail. Three coefficients are given for each sail; the lift coefficient C_L , the drag coefficient C_{D0} , and the quadratic parasitic drag C_{DQ} . Induced drag is not included in the force coefficients.

The current CFD-VPP implementation requires a table describing the aggregate sail force coefficients as a function of the apparent wind angle β_A . Thus, the individual sail force coefficients must be pre-assembled for each sailset.

This is done with a modified version of the procedure presented in ORC (2017). For C_L and C_{D0} the sum is weighted by sail area. For the quadratic parasitic drag C_{DQ} , the sum is weighted by sail area multiplied with lift coefficient squared.

$$C_L = \frac{\sum C_{L,i} A_i}{A} \quad (6)$$

$$C_{D0} = \frac{\sum C_{D0,i} A_i}{A} \quad (7)$$

$$C_{DQ} = \frac{\sum C_{DQ,i} A_i C_{L,i}^2}{A C_L^2} \quad (8)$$

The induced drag coefficient C_{DI} is computed based on the aggregate lift coefficient C_L and the effective aspect ratio Λ_E , as is shown in Equation 9. The effective aspect ratio Λ_E is computed from the sailplan span S , aggregate sail area A and apparent wind angle β_A , according to Equation 10.

$$C_{DI} = \frac{C_L}{\pi\Lambda_E} \quad (9)$$

$$\Lambda_E = \frac{S^2}{A} \left[1 + 0.1 \left(1 - \min \left[\max \left(\frac{\beta_A - 30}{60}, 0 \right), 1 \right] \right) \right]^2 \quad (10)$$

After the contribution from the individual sail have been summed up, the total drag coefficient C_D is obtained by adding the induced drag and the quadratic parasitic drag. The aggregate sail coefficients, C_L and C_D for the up- and downwind sailsets are shown in Figure 7.

$$C_D = C_{D0} + C_{DI} + C_{DQ} \quad (11)$$

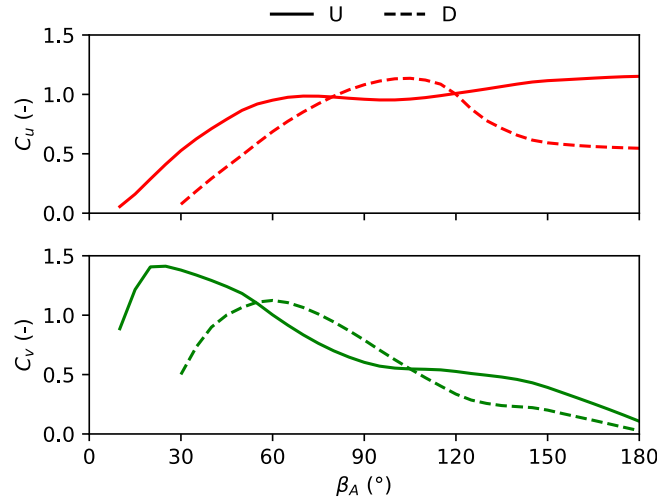


Figure 7: Aggregate sail coefficients for up- and downwind sailsets

The thrust coefficient C_u and side force coefficient C_v are determined as per equations 12 and 13.

$$C_u = C_L \sin \beta_A - C_D \cos \beta_A \quad (12)$$

$$C_v = C_L \cos \beta_A + C_D \sin \beta_A \quad (13)$$

The thrust F_u and side force F_v are then computed as shown in equations 14 and 15. The computed sail forces are then applied in the centre of effort CE (see section 2.2.1).

$$F_u = 0.5 \rho_a V_A^2 C_u A \quad (14)$$

$$F_v = 0.5 \rho_a V_A^2 C_v A \quad (15)$$

2.2.4 Rudder Angle Control

The rudder angle must be adjusted for each sailing condition to ensure yaw balance. This is achieved with a PID controller. In general terms, a PID controller determines a new value for a controlled variable based on the sum of the proportional (P), integral (I) and derivative (D) terms of the error. For the purpose of rudder control, the error e corresponds to the yaw moment residual. The controlled variable is the rudder angle δ .

The rudder angle controller is a discrete implementation of a standard form PID controller Trevathan (2006), operating in velocity mode, computing the change in controller output, as shown in Equation 16, where K_p is the proportional gain, K_I is the integral gain and K_D is the derivative gain.

$$\Delta\delta(t) = \left(K_p + K_I\Delta t + \frac{K_D}{\Delta t} \right) e(t) - \left(K_p - 2\frac{K_D}{\Delta t} \right) e(t-1) + \left(\frac{K_D}{\Delta t} \right) e(t-2) \quad (16)$$

A discrete, velocity mode controller avoids the need to compute integral and derivative values of the error. Instead, it only requires the error to be known at the current and the two previous time steps.

The controller must be tuned, i.e. values for K_p , K_I and K_D must be determined. The individual terms of the controller (i.e. proportional, integral or derivative), can be disabled by setting the corresponding gain coefficient to zero. The gain coefficients used in the CFD-VPP are shown in Table 7.

Table 7: Gain coefficients

K_p [-]	K_I [-]	K_D [-]
0	-0.001	0

Since K_I is the only non-zero gain coefficient, the implemented rudder controller is working in integral-only mode. Integral mode is sufficient to eliminate steady-state error, but may cause large overshoot of the rudder angle, as well as delayed response to dynamic events (Trevathan, 2006).

The current value for K_I has been determined using a trial-and-error process, with the objective of achieving zero steady-state error in a reasonable time.

2.2.5 Initialisation Procedure, Convergence Criteria and True Wind Angle Stepping

In order to reduce the time required for the simulation to reach steady state convergence, an initialisation procedure where the forces are smoothly ramped is used.

Due to the sudden application of a forward velocity to the body, an initial transient occurs with very high fluid forces in the first time step. To ensure that this does not start oscillation and/or divergence of the rigid body motions, the body is initially fixed in all degrees of freedom, and released after 0.1 s of simulation time. At this time, the rudder controller is also activated.

After the release of the body, the fluid forces are smoothly ramped, with a half-sinusoidal ramp function, so that the full fluid forces are applied to the rigid body after 5 s of simulation time.

The simulation is then time stepped to reach convergence for a specific combination of β_T and V_T . The monitored variables are boat speed V_B , heel angle ϕ , leeway angle λ and rudder angle δ . Convergence is considered to be achieved when all of these variables are asymptotic within 0.1 kn or 0.1° over 1 s of simulation time.

When convergence is reached, the true wind angle β_T is updated. The simulation is then restarted from the converged condition for the previous β_T , and again run until the convergence criteria is satisfied. Restarting from a previously converged state minimizes the simulation run time, since the difference in the state variables between two subsequent wind angles is likely to be small.

This procedure is then automatically repeated for the specified range of true wind angles, which means that an entire polar plot can be computed without user intervention. For each true wind angle the complete CFD solution is saved, along with tabulated results for the state variables (see Table 8). Computations for one true wind speed, five true wind angles and one sailset can be completed in 56 hours on a Linux HPC cluster, with 256 CPU cores allocated.

3. PROOF OF CONCEPT

The performance and suitability of the modified procedure has been evaluated with performance predictions on the SYRF 14 m yacht. In order to limit the computational resources consumed, predictions have only been done for one true wind speed, $V_T = 10$ kn. For this true wind speed, a range of several true wind angles have been computed, including both up- and downwind sailsets. All computations are performed in static conditions, with steady wind and calm water.

One important aspect of the modified procedure is that correct alignment between grid and free surface is maintained even for large heel angles. In Figure 8, the volume fraction of water (red) is shown on a vertical plane section. This shows how the background grid stays aligned with the free surface when the yacht heels.

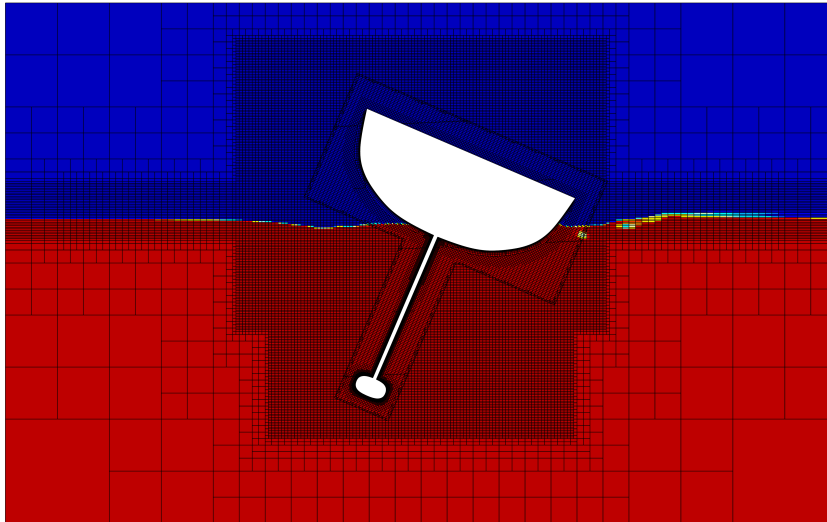


Figure 8: Vertical section showing volume fraction. Note that the free surface and grid remains aligned at large heel angles.

Figure 9, shows the free surface wave pattern generated by the SYRF 14 m yacht at $V_T = 10$ kn and $\beta_T = 45^\circ$. The sail force is indicated by the black arrow. Since the grid remains aligned with the free surface, the wave pattern can be resolved in detail, without artifacts, even at the relatively high angle of heel seen for this condition.

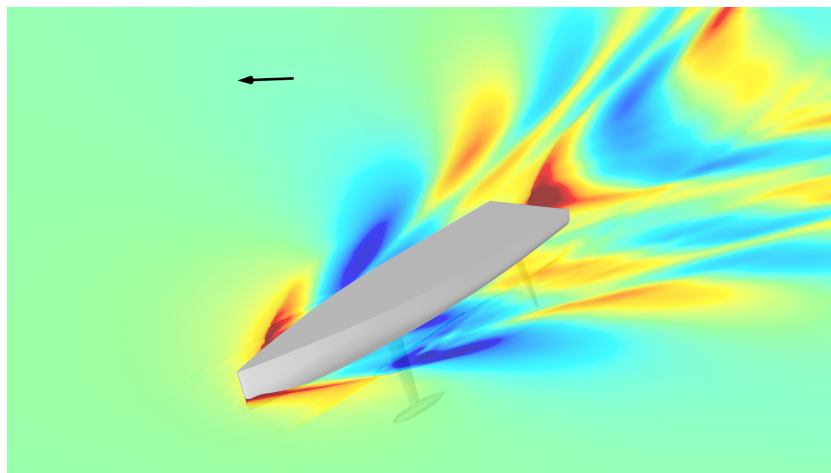


Figure 9: Free surface wave pattern at $V_T = 10$ kn and $\beta_T = 45^\circ$. The aggregate sail force is shown by the black arrow.

3.1 Convergence History

In Figure 10, the convergence history for a typical upwind solution, at $\beta_T = 45^\circ$ and $V_T = 10$ kn is shown. The monitored variables are those used in the convergence criteria; boat speed V_B , heel angle ϕ , leeway angle λ and rudder angle δ .

The initialisation procedure releases all DOF's after 5 s of simulated time. This causes some initial oscillations, which are quickly damped. For heel, leeway and rudder angle, only small oscillations ($< \pm 0.05^\circ$) remain at 30 s. The boat speed is converged to within ± 0.05 kn in 30 s simulated time.

This can be compared to Levin and Larsson (2017) where all DOF's are released after 40 s, and a total of 100 s simulated time is required to reach oscillatory convergence.

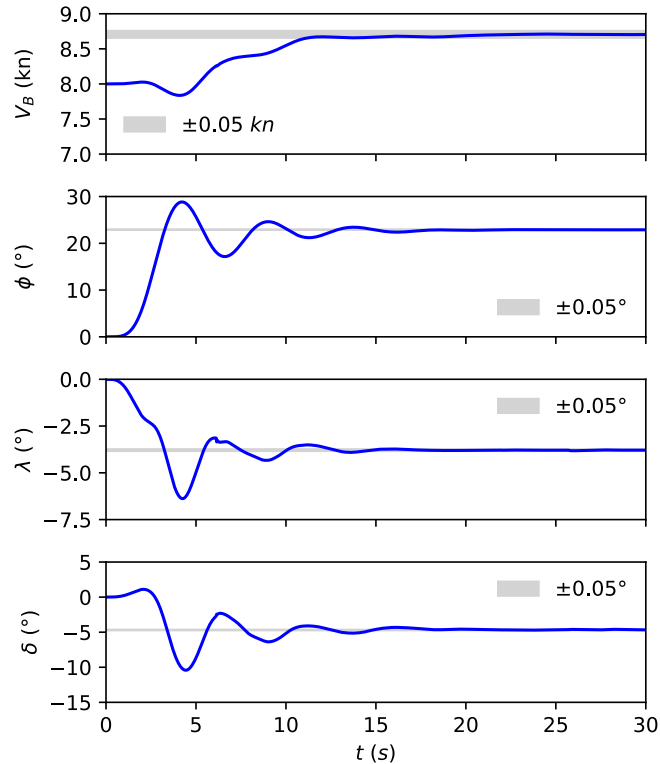


Figure 10: Convergence history for speed, heel, leeway and rudder angles.

3.2 Performance Prediction Results

Figure 11 shows a polar plot for the SYRF 14 m yacht, where boat speed, as predicted with the CFD-VPP, is presented as a function of true wind angle β_T , at a true wind speed of $V_T = 10$ kn. Predictions for both up- and downwind sailsets are shown.

For reference, results from the ORC-VPP for a Ker 46 is also shown ORC (2019). This yacht has similar main particulars, including length, beam, draft, displacement and sail area. Thus, their performance potential could be expected to be similar.

For close-hauled and downwind conditions, the CFD-VPP results for the SYRF 14 m yacht agree well with the ORC-VPP results for the Ker 46. However, for close- and beam-reaching angles, with the upwind sailset, the CFD-VPP seems to overpredict boat speed. The reason for this has not yet been investigated.

In Table 8, numerical results are shown, tabulated for true wind angle β_T . The results show a systematic trend across true wind angles, with all state variables within reasonable bounds. The rudder angles show moderate weather helm, indicating that a reasonable estimate for the CE has

Table 8: Results from velocity prediction at $V_T = 10$ kn.

β_T [°]	V_A [kn]	β_A [°]	V_B [kn]	ϕ [°]	λ [°]	δ [°]
30	16.7	14.9	7.5	17.7	-4.4	-2.8
45	16.7	21.4	8.5	22.3	-3.9	-4.8
60	16.4	28.2	9.5	21.3	-2.7	-4.9
90	13.8	44.5	9.8	10.6	-1.4	-2.2
120	9.2	68.3	8.4	0.1	-0.8	-0.5
90	12.9	42.7	9.5	24.5	-3.0	-4.0
120	9.5	60.4	9.7	11.9	-1.5	-1.2
135	7.2	74.2	9.0	3.8	-1.1	-0.1
150	5.0	98.3	7.9	-1.5	-0.5	0.3
165	4.7	146.7	5.8	-3.3	-0.3	0.1

been found.

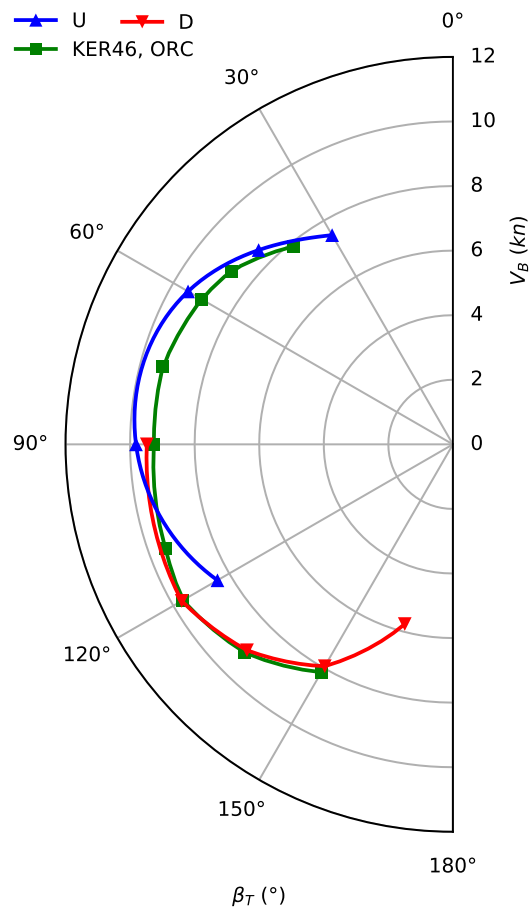


Figure 11: SYRF 14 m yacht polar plot at $V_T = 10$ kn.

4. CONCLUSIONS

In this paper, an improved procedure for strongly coupled prediction of sailing yacht performance is presented. The procedure is similar in principle to those presented by Roux et al. (2008), Boehm and Graf (2010) and Levin and Larsson (2017), but implementation details have been modified.

The modified procedure results in significantly improved convergence behaviour, reducing the required simulation time. In comparison to Levin and Larsson (2017), a more advanced rudder control algorithm has been implemented, eliminating rudder oscillation. A different configuration of the grid motion ensures that the grid remains aligned with the free surface, resulting in improved free surface discretisation.

The capabilities of the procedure were demonstrated with performance prediction for a modern 14 m sailing yacht. Comparisons with velocity predictions from the ORC-VPP for a similar yacht showed good agreement. One true wind speed, a range of true wind angles and two sailsets were considered. The computations were completed in approximately 120 hours, using 256 CPU cores, on a Linux HPC cluster.

5. FUTURE WORK

While this procedure is an improvement over those previously published, there are several areas which need to be developed. This work is currently in progress.

A grid dependence study will be performed to ensure that the grid resolution is sufficient to predict resistance, side-force and moments at a low uncertainty. Recently introduced adaptive grid methods will be utilized to reduce the need for volumetric refinements surrounding the overset interfaces, which could potentially provide a dramatic reduction in grid size.

Sail depowering routines are common in conventional VPP's. Since the yacht is overpowered in certain conditions, functions for sail flattening, twisting and reefing are to be implemented in the CFD-VPP. Routines for controlling crew righting moment will also be introduced.

While the sail model is quasi-static, and thus should be suitable for use in dynamic conditions, the integral-only rudder controller is unsuitable. Proportional and derivative terms will be included to provide adequate control of rudder angle in dynamic conditions (Trevathan, 2006).

In order to improve prediction accuracy, albeit with reduced generality, an alternative sail force model could be implemented. Such a model could use yacht specific sail force coefficients precomputed with RANS CFD. A long-term alternative could be to resolve the aerodynamic flow around the sails within the CFD-VPP. However, this would incur additional computational effort, and since the required sail trim varies significantly depending on wind speed and angle, a routine for morphing the sail shape would have to be included.

6. ACKNOWLEDGEMENTS

This research was performed in the project *Accurate Performance Prediction for Sail-Assisted Ships* and is funded by the Swedish Energy Agency (project no. P47469-1) and the Chalmers Foundation.

The computations were performed on resources at the National Supercomputer Centre (NSC) and Chalmers Centre for Computational Science and Engineering (C3SE), provided by the Swedish National Infrastructure for Computing (SNIC).

REFERENCES

- R. Azcueta and R. Schutt. 6 Degree of Freedom CFD Applied to the Design of an IMOCA Open 60. In *Proceedings of the Second International Conference on Innovation in High Performance Sailing Yachts*, Lorient, France, 2010.
- C. Boehm and K. Graf. Coupling of RANSE CFD with VPP Methods: From the Numerical Tank to Virtual Boat Testing. In *Proceedings of the Second International Conference on Innovation in High Performance Sailing Yachts*, Lorient, France, 2010.
- J. Choi and S. B. Yoon. Numerical simulations using momentum source wave-maker applied to RANS equation model. *Coastal Engineering*, 56(10):1043–1060, October 2009. ISSN 03783839. doi: 10.1016/j.coastaleng.2009.06.009.
- L. Larsson, R. Eliasson, and M. Orych. *Principles of Yacht Design*. Adlard Coles Nautical, London, UK, 2014. ISBN 9781408187906.
- R. L. Levin and L. Larsson. Sailing Yacht Performance Prediction based on Coupled CFD and Rigid Body Dynamics in 6 Degrees of Freedom. *Ocean Engineering*, 144:362–373, November 2017. ISSN 00298018. doi: 10.1016/j.oceaneng.2017.09.052.
- Offshore Racing Congress ORC. *ORC VPP Documentation*, 2017.
- Offshore Racing Congress ORC. ORC International Certificate 19360a, 2019. Ker 46 (FRA-3600).
- Y. Roux, A. Leroyer, M. Visonneau, J. Raymond, and F. Hauville. Strongly Coupled VPP and CFD RANSE Code for Sailing Yacht Performance Prediction. In *Proceedings of the 3rd High Performance Yacht Design Conference*, Auckland, New Zealand, 2008.
- Sailing Yacht Research Foundation. 14 meter hull, 2017. <http://www.sailyachtresearch.org/projects/14meterhull/>.
- V. L. Trevathan. *A Guide to the Automation Body of Knowledge (2nd Edition)*, pages 35–36. 2006. ISBN 978-1-55617-984-6.